A COUPLED CREEP PLASTICITY MODEL FOR RESIDUAL STRESS RELAXATION OF A SHOT PEENED NICKEL-BASE SUPERALLOY

Dennis J. Buchanan[2], Reji John[1], Robert A. Brockman[2], Andrew H. Rosenberger[1]
[1]Materials and Manufacturing Directorate
Air Force Research Laboratory (AFRL/RXLMN)
Wright-Patterson AFB, OH 45433-7817
[2]University of Dayton Research Institute
Dayton, OH 45469-0020

Keywords: creep, shot peening, residual stress relaxation, modeling, Ni base superalloy, IN100

Abstract

Shot peening is a commonly used surface treatment process that imparts compressive residual stresses into the surface of metal components. Compressive residual stresses retard initiation and growth of fatigue cracks. During the component loading history, the shot-peened residual stresses may change due to thermal exposure, creep, and cyclic loading. In these instances, taking full credit for compressive residual stresses would result in a nonconservative life prediction. This paper describes a methodical approach for characterizing and modeling residual stress relaxation under elevated temperature loading, near and above the monotonic yield strength of IN100. The model incorporates the dominant creep deformation mechanism, coupling between the creep and plasticity models, and effects of prior plastic strain. The initial room temperature residual stress and plastic strain profiles provide the initial conditions for relaxation predictions using the coupled creep-plasticity model. Model predictions correlate well with experimental results on shot-peened dogbone specimens subject to single cycle and creep loading conditions at elevated temperature. The predictions accurately capture both the shape and magnitude of the retained residual stress profile.

Introduction

In addition to the metallurgical advancements in chemistry, melting, and processing techniques, surface treatments such as shot peening (SP), low plasticity burnishing (LPB) and laser shock peening (LSP) have been employed to enhance damage tolerance by imparting compressive surface residual stresses at fracture-critical locations [1,2]. Compressive residual stresses retard crack initiation and growth, resulting in improved fatigue performance. Numerous studies [3-10] on steels, titanium and nickel-base superalloys have shown that residual stresses generated via surface treatment relax when subjected to elevated temperature exposure or mechanical loading. A variety of sophisticated empirical models have been developed and shown to capture trends in residual stress relaxation [5-7,10]. However, material microstructure, hardening behavior, plastic strain, and the underlying physical deformation mechanisms responsible for stress relaxation are not incorporated into many of these models. The result is a relaxation model that must be recalibrated for each surface treatment process and associated control parameters.

Surface treatment processes such as SP, LSP and LPB produce three important changes in the near surface layers of the material: (1) hardening of the material, i.e., raising the yield strength; (2) large biaxial compressive surface residual stresses constrained by small compensatory tensile stresses distributed through the bulk of the body, and (3) an unstable dislocation structure near the free surface. The surface treatment deformation results in plastic strain, yield surface, and residual stress profiles that change as a function of depth from the surface. Most residual stress relaxation models in the literature only account for item (2), the initial state of residual stress in the structure. Unfortunately, shot peening produces a highly deformed and stressed dislocation structure that is easily perturbed by thermal exposure or mechanical loading. Items (1) and (3) must also be incorporated in the experiments and as initial conditions in the models so that residual stress relaxation of other surface treatment processes, such as LSP and LPB, can be included in a deformation mechanism based approach.

Creep Deformation Mechanisms and Models

Creep deformation mechanisms in metals may be grouped into a number of broad categories depending on the author [12,13]. Under low stress and high temperature conditions bulk diffusion through the lattice (Nabarro-Herring Creep) dominates, while for low stress and moderate temperatures diffusion along grain boundaries (Coble Creep) becomes the dominant deformation mechanism. At higher stresses and low to moderate temperatures, less than 0.3 Tm (Tm = melting temperature), deformation is controlled by dislocation glide. For temperatures above 0.3 Tm, the mobility of vacancies allows dislocations to climb out of the current glide plane to one of less resistance, thereby increasing the creep rate. Finally, for stresses that reach the theoretical or ideal strength of the crystal, approximately equal to G/30, the material becomes unstable and fractures.

The primary variables associated with creep deformation and creep rate are stress, temperature and time. Much of the early work characterizing creep behavior has been aimed at fitting empirical equations to a general form where it has been typically assumed that the functions for stress, temperature and material properties are separable into a product as

$$\varepsilon_c = F_1(\sigma)F_2(T)F_3(t) \qquad (1)$$

This approach may be acceptable when stress, temperature and material properties do not change with time. For variable stress and temperature loading conditions a rate formulation must be adopted. The creep strain rate equation is often cast in either a time hardening,

$$\dot{\varepsilon}_c = F_1(\sigma)F_2(T)F_3(t) \qquad (2)$$

or strain hardening formulation:

$$\dot{\varepsilon}_c = F_1(\sigma)F_2(T)F_4(\varepsilon_c) \qquad (3)$$

Both are state variable approaches that may be applied to complex thermomechanical loading histories. The time hardening formulation is somewhat cumbersome to implement in that the origin in time must be reset for each stress increment. The strain hardening approach has the additional advantage that time is not included as an independent variable in the model. For these reasons, most creep analyses implement a strain hardening formulation.

A major element missing from the above creep models is the evolution of material microstructure with time or deformation history. It is almost always assumed that the microstructure and hence the material properties remain unchanged throughout the deformation history. Aspects of the material microstructure such as grain size, dislocation structure, inclusions, vacancies, etc. all have an impact on the deformation rate. Both the time hardening and strain hardening approaches are suitable if the creep rate is dominated by a single deformation mechanism. If multiple deformation mechanisms are active, or the dominant mechanism changes with thermal and mechanical loading history, simple time and strain hardening approaches fail to capture the loading response. Schoeck [12] presents a more general formulation for creep rate that accounts for multiple independent creep mechanisms in the form

$$\dot{\varepsilon}_c = \sum_i f_i(\sigma, T, st)e^{-U_i(\sigma, T, st)/kT} \qquad (4)$$

where

f_i = creep rate function (i.e., creep mechanism),
U_i = activation energy for creep mechanism,
σ = applied stress,
T = temperature,
k = Boltzmann's constant,
st = structure of the material.

This formulation addresses the evolution of a changing microstructure as a contributing factor to the creep rate, but implies the deformation mechanisms are independent. Numerous models have been developed for the dominant creep mechanisms such as glide and climb of dislocations, and diffusion through grains and along grain boundaries. Nowick and Machlin [14] and Weertman [15] developed the early dislocation creep models to describe climb and glide deformation mechanisms which gave rise to many of the commonly used exponential and hyperbolic sine formulations for creep rate. The interaction or competition between deformation mechanisms can become complex. Initial approaches to represent material degradation under creep loading include the continuum damage mechanics (CDM) approaches of Kachanov [16] and Rabotnov [17] that incorporate a single damage parameter and associated evolution equation. More recently, the simple damage parameters in the CDM approach have been replaced by specific degradation models representing mechanisms such as cavity nucleation and growth, subgrain coarsening, multiplication of mobile dislocations, and thermally and environmentally driven mechanisms [18-24].

A number of modeling approaches have been developed to account for the combined contributions of plasticity and creep [18-20,25-29]. The trend has been to incorporate plasticity and creep into a single unified inelastic model. The unified models have evolved to include complex nonlinear hardening rules to capture the Bauschinger effect, and cyclic hardening or softening. Unfortunately, the microstructural deformation mechanisms behind creep and plastic deformation, which are fundamentally different, have been combined in this approach.

Investigations of the effects of prior room temperature prestrain on creep have been performed in copper [33], nickel [32,34] and aluminum [11]. Parker and Wilshire [33] show that tensile prestrain of 5 to 12.5 percent change both the primary and secondary creep rates, and that the secondary creep rate decreases with increasing levels of prestrain. The experiments were conducted at a temperature of 0.7 Tm, in which dislocation enhanced diffusion is the rate-controlling mechanism. They also conclude that the primary deformation mechanism is independent of the level of prestrain. Davies et al. [32] investigated elevated temperature compressive prestrain of two to eleven percent on creep in pure nickel. In Davies' study the elevated temperature compressive prestrain increases secondary creep rate by an amount which is independent of the level of prestrain. Evans and Wilshire [11], using two aluminum alloys, demonstrated that in one material secondary creep rate increases with increasing levels of prestrain while in another material secondary creep rate decreases with increasing levels of prestrain, for identical temperatures but different stress ranges. They reason that if the primary deformation mechanism is recovery or climb controlled, then increasing levels of prestrain would result in lower secondary creep rates. If the primary deformation mechanism is glide controlled, then increasing levels of prestrain would result in higher secondary creep rates. In all cases, prior prestrain does affect the subsequent creep rate. The experiments indicate that the level of prestrain, the direction (tensile or compressive) and the dominant deformation mechanism all contribute to whether creep rate increases or decreases with increasing levels of prestrain.

Relaxation of Shot Peened Residual Stresses

Shot peening has been employed for decades to impart compressive residual surface stresses for retardation of crack initiation and crack growth. Numerous studies have characterized the beneficial effects of compressive residual surface stresses on fatigue life for aluminum-, titanium- and nickel-base alloys [1-2,5-6]. For applications that utilize aluminum and titanium alloys, subjected to moderate temperatures and stresses, residual stresses are assumed to be stable with repeated cyclic stress-controlled loading. In contrast, nickel-base superalloys are typically selected for applications where temperatures may reach 80 percent of the melting temperature, and stresses approach or exceed the monotonic yield strength. At elevated temperatures and high stress loading conditions, inelastic deformation will alter the original residual stress depth profile. Further, changes to the microstructure resulting from shot peening, long term elevated temperature exposure, and deformation history may accelerate the relaxation rate of residual stresses. Understanding the relaxation of residual stresses is necessary to improve the ability to predict service life of shot-peened components.

Thermal relaxation studies on shot peened steels [7], titanium alloys [3] and nickel alloys [3-4,6,8-9] have demonstrated that relaxation of residual stresses may occur at relatively low

temperatures and over short durations. Vöhringer and coworkers [7] recognized that in addition to temperature and exposure time, the state of the material microstructure is itself another parameter that affects relaxation rate of residual stresses. Cao and colleagues [6] developed a thermal recovery model based on the decreasing half-width of x-ray diffraction peaks which they attributed to annihilation and reorganization of crystalline defects. The thermal recovery was modeled as a macroscopic recovery strain that was a function of time and temperature. Prevéy [3,8] has characterized thermal relaxation behavior for a number of materials and surface treatment techniques and has concluded that the rate of relaxation is correlated to the degree of cold working. Prevéy [8] claims that laser shock peening (LSP) and low plasticity burnishing (LPB), which are termed low cold work surface treatment processes, are more resistant to thermal relaxation of residual stresses than conventional shot peening. Thermal relaxation measurements made on superalloy material extracted from retired turbine disks were fit with multi-linear regression analysis by Gabb et al. [4]. Analysis of this data indicated that residual stress relaxation increases with temperature, exposure time, and level of initial cold work.

Research into relaxation of residual stresses subject to mechanical loading has followed a much different path than thermal relaxation. For thermal relaxation, temperature and exposure time are the primary parameters, while for mechanical loading the important factors are temperature, maximum and minimum applied stress, loading frequency, hold time, waveform shape and number of applied cycles. Holzapfel et al. [7] describe residual stress relaxation consisting of three different stages: (1) relaxation due to specimen heating; (2) relaxation during the first cycle; and (3) relaxation with the logarithm of cycle count. A similar approach by Cao et al. [6] describes thermomechanical relaxation as a two-stage process, in which the first stage is a shakedown of the initial residual stresses described by a monotonic stress strain law, and a second stage that is slower and is described by a cyclic softening related to the logarithm of number of the applied cycles.

For complex spectrum loading conditions, a full constitutive model that integrates the solution forward in time is necessary to capture the state of residual stress at each cycle. The most common formulation is the unified theory that incorporates plasticity, creep and recovery into a single viscoplastic model. Chaboche and Jung [10] and Ahmad et al. [5], using viscoplasticity models, predict residual stress relaxation in surface treated nickel-based superalloys at elevated temperature. The fundamental flaw in the unified models is the assumption that plasticity, creep and recovery can be combined into a single formulation. This approach contradicts experimental evidence that plasticity, creep and recovery are different deformation mechanisms and as such must be modeled separately, but possibly coupled.

Prevéy [3,8] argues that the rate of residual stress relaxation and amount of relaxation is directly correlated to the level of cold work in surface-treated Ti-6Al-4V and IN718. Prevéy's measurements on IN718 made via x-ray diffraction line broadening show that at the surface, LSP and LPB have less than 10 percent cold work, while shot peening cold work approaches 40 percent for similar peak compressive residual stresses [8]. However, shot peening cold work drops to nearly zero at a depth of 100 μm, while LPB becomes nearly zero at 1000 μm, and LSP exhibits approximately two to three percent cold work to a depth

of over 1400 μm [8]. Clearly, the depth of plastic strain and not just the surface value contribute to the relaxation of residual stresses induced by surface treatments.

Therefore, an approach that incorporates both the plastic strain (cold work) and the residual stress depth profiles is required to model relaxation of residual stresses for a multitude of surface treatment processes.

Material Description of IN100

IN100 is a powder metal (PM) nickel-base superalloy. The nominal chemical composition of IN100 is 12.4Cr, 18.5Co, 4.7Ti, 5.5Al, 3.2Mo, 0.8V, and 0.07C (wt %). IN100 has a face-centered cubic (FCC) structure with an average grain size of approximately 25μm. In FCC structures such as this IN100 alloy there are aluminum (Al) atoms at the crystal corners and nickel (Ni) in the center of each face of the crystal which make up the Ni_3Al structure. The microstructure is composed of a continuous gamma (γ) matrix, and precipitate cubical gamma prime (γ'). The cubical gamma prime is responsible for the excellent creep resistance of this alloy. The gamma prime is strong and ductile which limits dislocation interaction and movement through the microstructure. Microstructural studies comparing IN100 samples thermally exposed for 300 hours at 704°C with baseline samples (no exposure) reveal no evidence of grain growth, no gamma prime coarsening, and no new phases detected. These same observations are also true for the heavily cold worked surface layers of the shot peened IN100 samples. Additional details about the baseline microstructure are described in the literature [31].

The monotonic true stress – true stain response for IN100 at two temperatures, 23°C and 650°C, is shown in Figure 1. Although the elastic modulus and ultimate tensile strength are dependent on temperature, the 0.2 percent yield strength and strain to failure are similar at 23°C and 650°C.
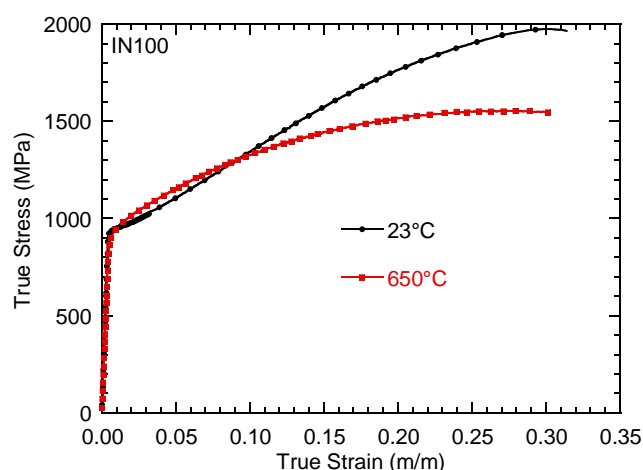

Figure 1. Monotonic true stress-true strain behavior for IN100 at 23°C and 650°C.

Creep with Prestrain Behavior in IN100

Traditionally creep data for constant temperatures above 0.4 Tm and constant stress conditions are often shown in a plot similar to Figure 2. The abscissa is time, which starts after the sample has reached the target stress. The ordinates on the left and right sides

respectively, are total strain and strain rate. The solid black line represents total strain and the dotted blue line strain rate. The plot has three regions identified as primary, secondary, and tertiary. The creep rate in the primary region decreases until a minimum or steady-state strain rate is reached in the secondary region. The secondary region is defined by a constant or minimum creep rate. Finally, the tertiary region is defined by increasing strain rate until failure. What is not shown in this type of plot is the material response prior to reaching the desired creep stress. In most materials the response is elastic, and only the initial loading strain is plotted on the graph as the first point. However, nickel-base superalloys, and specifically IN100, have been developed to resist creep deformation at temperatures of 0.8 Tm, and stresses near and above the yield strength. Under these conditions, plastic yielding during loading will affect the creep rate and deformation response. Furthermore, if the material is subject to prior plastic strain at room temperature, elevated temperature yielding may be mitigated.

Figure 3. Strain rate versus total strain curves for IN100 under creep loading at σ=1000MPa & 650°C for different levels of room temperature plastic prestrain.

Table 1. Minimum creep rate as a function of plastic prestrain level and applied stress for IN100 at 650°C.

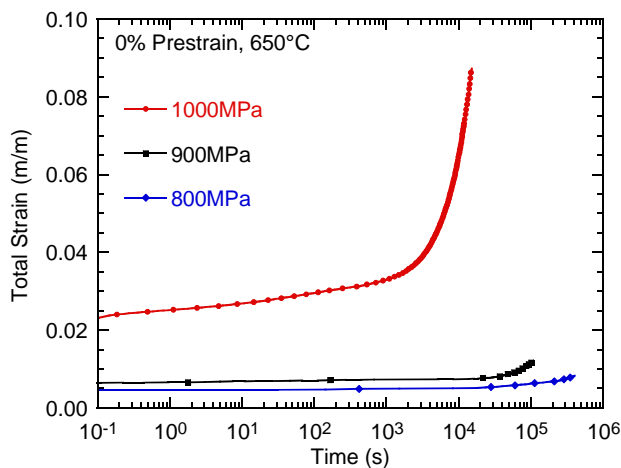| ε_{max} (MPa)	Minimum Creep Rate (m/m/s)			
	Plastic Prestrain Level (%) @ 23°C			
	-1	0	1	5
1000	1.05E-06	2.37E-06	3.98E-07	1.13E-07
900	2.24E-07	4.03E-09	3.66E-08	3.38E-09
800	8.90E-09	4.60E-09	-	3.40E-09

Figure 2. Total strain versus time curves for IN100 at 650°C.

The effect of room temperature plastic prestrain on creep deformation behavior is shown in Figure 3 for an applied stress of 1000 MPa and temperature of 650°C. The zero percent prestrain case is the baseline that has been discussed in previous plots. The one percent prestrain case exhibits delayed yielding resulting from an increase in the yield stress during prestrain loading. The minus one percent prestrain loading exhibits a lower tensile yield resulting from the Bauschinger effect and supports the need to include a plasticity model with kinematic hardening. Also, the increase in strain rate is more gradual for the compressive prestrain, which is consistent with the more gradual hardening curve described in the previous paragraphs on cyclic hardening. Only for the five percent prestrain test is yielding mitigated upon loading to 1000 MPa. The data also show that any prestrain, tensile or compressive, results in a decrease in the minimum strain rate. The open diamond symbols represent the initial loading strain, and clearly reflect the complex deformation that occurs prior to reaching the target stress for creep.
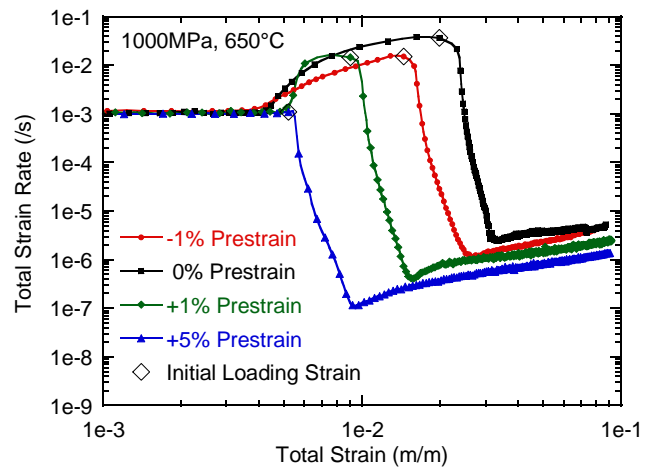
Coupled Creep-Plasticity Model

The constitutive model developed in this study is based on a rate-independent plasticity model, and a strain hardening creep model that is coupled to the plasticity model through the plastic strain rate and yield surface size. The plasticity model is based on the von Mises effective stress with a nonlinear mixed isotropic-kinematic hardening rule as described by Dodds [30]. The creep model follows the physics-based modeling of dominant deformation mechanisms similar to the approaches of Ashby, Dyson, McLean and others [13,21-24]. Based on the SEM and TEM observations of the shot peened and thermally exposed microstructure, it has been argued that the microstructure remains stable over the range of temperatures and exposure times in this study [38]. Therefore a microstructural model dominated by a single deformation mechanism is sufficient to model residual stress relaxation behavior. The elastic-plastic-creep model is cast in an implicit integration form suitable as a standard user material subroutine (UMAT) for implementation into ABAQUS/Standard. Details of the physical deformation mechanism, constitutive equations and solution procedure follow.

Identification of the primary creep deformation mechanism is required before development of a model may begin. One approach to determining the dominant mechanism is to fit the minimum creep rate versus stress data to a power law equation and evaluate the exponent of stress (n). Bulk diffusion through

the grain (Nabarro-Herring Creep) and diffusion along grain boundaries (Coble Creep) may be characterized by minimum creep rates that are directly proportional to stress raised to an exponent n = 1. Dislocation mechanisms such as climb and glide typically have a power law exponent that is higher and with a range of n = 3-5. The creep rate data from this study exhibit an exponent of n ≈ 6, and therefore dislocation motion is the primary deformation mechanism for the range of conditions evaluated. Furthermore the applied stresses of 800-1000 MPa which are at and above yield, and moderate temperature of 650°C (0.58*Tm) suggest that dislocation glide is dominant over dislocation climb which is a lower-stress, higher-temperature mechanism. Therefore a creep model with dislocation glide as the dominant deformation mechanism is chosen for this alloy and range of operating conditions.

Many of the viscoplastic models in the literature follow similar arguments about microstructural behavior in the development of the constitutive equation. However, unified models [5,18-19,25-29] that decompose the total strain rate into elastic and inelastic components as shown by

$$\dot{e}_{ij} = \dot{e}_{ij}^e + \dot{e}_{ij}^{in} \tag{5}$$

imply that plastic and creep deformation are one and the same mechanism. Decomposing inelastic behavior into two rate terms enables independent creep and plasticity deformation mechanisms to be incorporated as shown by

$$\dot{e}_{ij} = \dot{e}_{ij}^e + \dot{e}_{ij}^p + \dot{e}_{ij}^c \tag{6}$$

This approach allows for creep and plasticity with distinct mechanisms. In fact, they are not independent, but are coupled through a backstress tensor and dislocation mobility model which allows the creep strain rate to be dependent on plastic strain rate, plastic strain, and the yield surface size.

The development of the creep model follows the microstructurally based deformation mechanism approach of Dyson, McLean, and colleagues [21-23]. The basic model is adapted to incorporate the effects of prior plastic strain and coupling to the plasticity model. The 1D effective creep strain rate relation, based on glide of dislocations as the dominant deformation mechanism, is defined such that it is identical to the axial component under uniaxial loading,

$$\dot{\bar{\varepsilon}}^c = \dot{\varepsilon}_o \left(1 + \bar{\varepsilon}^{dm}\right) sinh\left(\frac{\bar{\sigma}}{\sigma_\kappa \kappa}\right) \tag{7}$$

where

$\dot{\bar{\varepsilon}}^c$ = effective creep strain rate,

$\dot{\varepsilon}_o$ = creep strain rate parameter,

$\bar{\varepsilon}^{dm}$ = effective mobile dislocation density,

$\bar{\sigma}$ = effective stress,

σ_κ = normalized stress parameter (nondimensional),

κ = size of yield surface.

The microstructural evolution equation for multiplication of mobile dislocations has been modified to incorporate the effect of plastic strain rate as follows:

$$\dot{\bar{\varepsilon}}^{dm} = M\dot{\bar{\varepsilon}}^p + N\dot{\bar{\varepsilon}}^c \tag{8}$$

Parameters M and N are coefficients that determine the contributions of plastic strain rate and creep rate toward the increase in dislocation mobility, respectively. In the absence of plastic strain, Equation 8 reduces to the damage rate equation described by McLean and Dyson [21].

The backstress rate $(\dot{\alpha}_{ij})$ is decomposed into components representing yield surface translation $(\dot{\alpha}_{ij}^p)$, creep backstress $(\dot{\alpha}_{ij}^c)$, and creep recovery $(\dot{\alpha}_{ij}^r)$,

$$\dot{\alpha}_{ij} = \dot{\alpha}_{ij}^p + \dot{\alpha}_{ij}^c - \dot{\alpha}_{ij}^r \tag{9}$$

The creep backstress evolution equation is adapted from the nonlinear kinematic hardening rule developed by Armstrong and Frederick [35] for plasticity,

$$\dot{\alpha}_{ij}^c = \frac{2}{3} C_c \dot{\varepsilon}_{ij}^c - \gamma_c \alpha_{ij}^c \dot{\bar{\varepsilon}}^c \tag{10}$$

with parameters for strain hardening (C_c) and strain softening (γ_c). The recovery evolution model,

$$\dot{\alpha}_{ij}^r = C_1 \alpha_{ij}^p \dot{\bar{\varepsilon}}^p \tag{11}$$

is strictly a function of plastic material behavior and is analogous to the strain softening term in Equation 10. Plastic hardening rules follow the approach in Dodds [30] in the form:

$$\dot{\alpha}_{ij}^p = \frac{2}{3} H'(1-\beta)\dot{\varepsilon}_{ij}^p \tag{12}$$

$$\dot{\kappa} = \beta H'(\varepsilon^p)\dot{\bar{\varepsilon}}^p \tag{13}$$

This formulation incorporates the Bauschinger effect with a mixed nonlinear isotropic-kinematic model where β defines the fraction of isotropic hardening and H' is the plastic modulus. Pure isotropic hardening occurs when β = 1 and pure kinematic hardening when β = 0.

As is typical for metals, it is assumed that hydrostatic stresses have negligible effect on yield behavior and that during plastic flow the material is incompressible. Therefore all constitutive equations have been based on deviatoric forms of the stress and strain tensors as shown below.

$$s_{ij} = \sigma_{ij} - \frac{\sigma_{kk}}{3}\delta_{ij} \tag{14a}$$

$$e_{ij} = \varepsilon_{ij} - \frac{\varepsilon_{kk}}{3}\delta_{ij} \qquad (14b)$$

The elastic relationship between stress and strain, shown below in deviatoric form, is the basis for integrating the stresses to the end of the time step.

$$\dot{s}_{ij} = 2G\dot{e}_{ij}^{e} \qquad (15)$$

Combining the elasticity equation with the additive strain rate, Equation 6, provides an equation for the dependent stresses in terms of the independent strain rates as,

$$\dot{s}_{ij} = 2G\left(\dot{e}_{ij} - \dot{e}_{ij}^{p} - \dot{e}_{ij}^{c}\right) \qquad (16)$$

We adopt Prandtl-Reuss flow equations for both plasticity and creep rate, identifying $\dot{\lambda}_p$ and $\dot{\lambda}_c$ as positive scalar quantities representing the different deformation histories,

$$\dot{e}_{ij}^{p} = \dot{\lambda}_p\left(s_{ij} - \alpha_{ij}^{p}\right) \qquad (17a)$$

$$\dot{e}_{ij}^{c} = \dot{\lambda}_c\left[s_{ij} - \left(\alpha_{ij}^{p} + \alpha_{ij}^{c} - \alpha_{ij}^{r}\right)\right] \qquad (17b)$$

The effective plastic strain rate, effective creep rate and von Mises effective stress are defined respectively as,

$$\dot{\bar{\varepsilon}}^{p} = \sqrt{\frac{2}{3}\dot{e}_{ij}^{p}\,\dot{e}_{ij}^{p}} \qquad (18a)$$

$$\dot{\bar{\varepsilon}}^{c} = \sqrt{\frac{2}{3}\dot{e}_{ij}^{c}\,\dot{e}_{ij}^{c}} \qquad (18b)$$

$$\bar{\sigma} = \sqrt{\frac{3}{2}\left(s_{ij} - \alpha_{ij}\right)\left(s_{ij} - \alpha_{ij}\right)} \qquad (18c)$$

The nonlinear stress-strain equation that relates the effective plastic strain to the von Mises effective stress is best described by a simple empirical equation as shown by,

$$\bar{\sigma} = \sigma_o + K\left(\bar{\varepsilon}^{p}\right)^{n} \qquad (22)$$

where σ_o is the virgin yield strength, K is the strain hardening coefficient, and n is the strain hardening exponent.

Integration of the solution forward in time starts by estimating the creep strain increment for the current material point based on the stress state and state variables at the beginning of the step. The predicted creep strain increment is subtracted from the supplied total strain increment to produce an elastic-plastic strain increment. An elastic-plastic solution follows to calculate an effective plastic strain increment and the stresses at the end of the time step, based on the predicted elastic-plastic strain increment. Then a corrected creep strain increment is calculated based on stresses calculated at the midpoint of the step. The corrected

creep strain increment is used to calculate an improved prediction for state variables at the end of the step. The correction procedure is repeated until the difference between the predicted and corrected stresses at the end of the step reaches a specified tolerance limit. If more than a specified number of corrections are needed to achieve the tolerance, a request to cut the time step is returned to ABAQUS. The solution for the elastic-plastic portion of the model follows the work of Braisted and Brockman [36] on a rate-dependent implicit model for Ti-6Al-4V. The solution was adapted to a rate-independent nonlinear isotropic-kinematic hardening model described by Dodds [30].
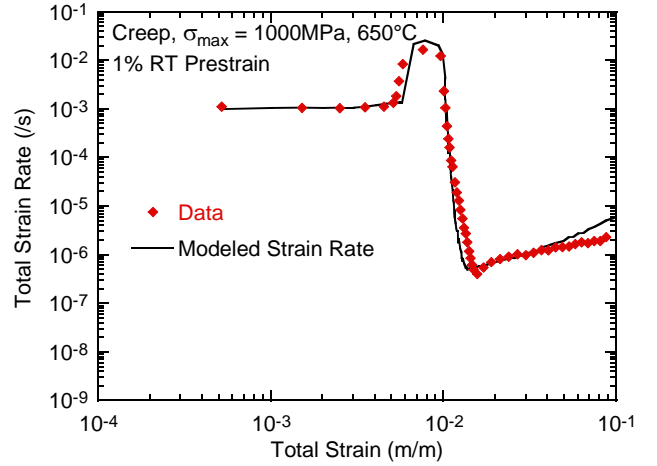

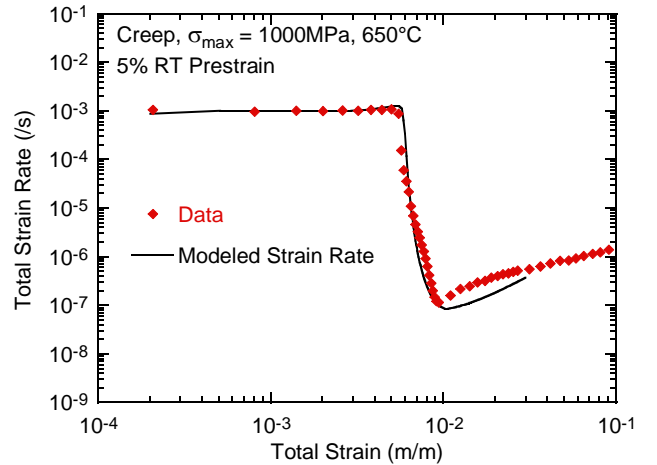Figure 4. Total strain rate versus total strain curves for IN100 under creep loading at σ=1000MPa, 1% RT plastic prestrain, and at 650°C.

Figure 5. Total strain rate versus total strain curves for IN100 under creep loading at σ=1000MPa, 5% RT plastic prestrain, and at 650°C.
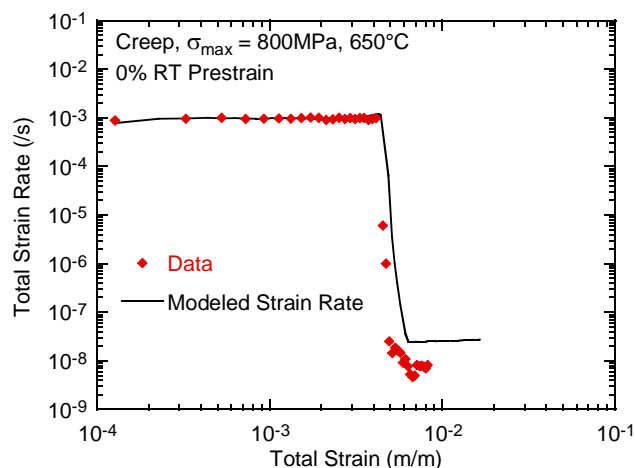
Figure 6. Total strain rate versus total strain curves for IN100 under creep loading at σ=800MPa, 0% RT plastic prestrain, and at 650°C.

Application of Coupled Model to Residual Stress Relaxation

Shot Peened Specimen Geometry

Characterization of the initial residual stress and plastic strain depth profiles are necessary for accurate prediction of the evolution of stresses and plastic strains under applied thermal and mechanical loading. The accuracy of stress predictions depends on accuracy of the initial conditions, specifically residual stresses and plastic strains. There are numerous variables that affect the residual stress and plastic strain depth profile. Elastic and inelastic material properties of the material itself have a pronounced effect on the resulting residual stresses and plastic strains. For example, machining and surface finishing processes, such as grinding and polishing, performed prior to shot peening all impart residual stresses into the component. The shot peening process itself has many factors that contribute to the variability of imparted residual stresses, including shot size, hardness, coverage and angle, just to mention a few. Figure 7 is a backscatter SEM micrograph of a polished cross section of IN100. The left side of the image is the shot peened surface of the sample. The left 50 μm area shows a distinct change in microstructure resulting from the shot peening-induced deformation. The right side shows the interior, with a typical representation of the microstructure and individual grains. Superimposed over the microstructure are representative residual stress and percent cold work (plastic strain) depth profiles determined by x-ray diffraction (XRD).

Identifying the steps involved in specimen machining, shot peening, mechanical testing, XRD and electropolishing, and analysis of the experiments is necessary to develop an integrated research plan. After identifying limiting factors such as material availability, size of test matrix, and experimental and analytical requirements, a rectangular cross section, dogbone geometry as shown in the left image of Figure 8. A large flat shot peened surface is desired to maximize the size of the irradiated region during XRD. A cylindrical geometry of equal cross sectional area would provide a much smaller surface area for XRD measurement, add complexity in measuring stresses on curves surfaces, and make electropolishing and measuring uniform layer removal for depth profiles more difficult. For the flat dogbone geometry an irradiated x-ray region of 3 x 5 mm with nominal

grain size of 25 μm provides approximately 30,000 interrogated grains over which to determine an average residual stress. A specimen width of 10 mm in the gage section provides a 3.5 mm border around the uniformly stressed region for residual stresses to decay to zero at the free surface. A specimen thickness of two mm was selected based on guidance from the shot peening vendor and the capacity of the hydraulic grip hardware.

Based on residual stress depth profiles on a similar superalloy, IN718 [3,8] and typical shot peening specifications for turbine engine components [1,2], an Almen intensity of 6A has been selected.
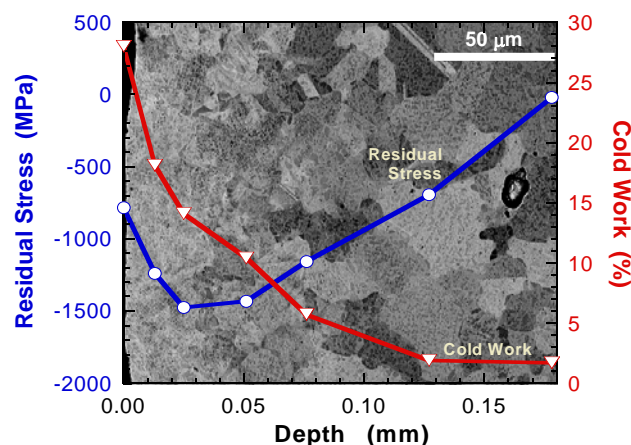

Figure 7. Composite of baseline residual stress and cold work depth profiles overlaid on shot peened microstructure.

Finite Element Model of Shot Peened Specimen Geometry

The flat dogbone specimen geometry described in the previous section has been designed with both experimental and analytical considerations in mind. The large flat surface of the dogbone sample provides a uniform state of stress in the plane of the sample over an area sufficient for averaging XRD measurements as a function of depth into the sample. The steep gradient and shallow depth of the residual stress profile of shot peening requires an element thickness less than five microns at the surface to accurately represent the stress distribution. Therefore a relatively simple and small geometry is desirable, given the required element size.

Figure 8 is an illustration of the dogbone specimen, an enlarged view of the gage section, and a core of the gage section that represents the geometry of the finite element model. The actual model exploits symmetry so only a half-thickness geometry is used for the analysis. The dimensions of the finite element geometry are 100 μm x 100 μm x 1 mm. Uniform displacement boundary conditions are enforced on the surface of the model. This is a reasonable assumption given that the tractions applied to the specimen grip section are far from the gage section. Also, the shot-peened layer is a small fraction of the depth (approximately one tenth), and therefore will provide negligible resistance to the bulk of the thickness deforming uniformly.
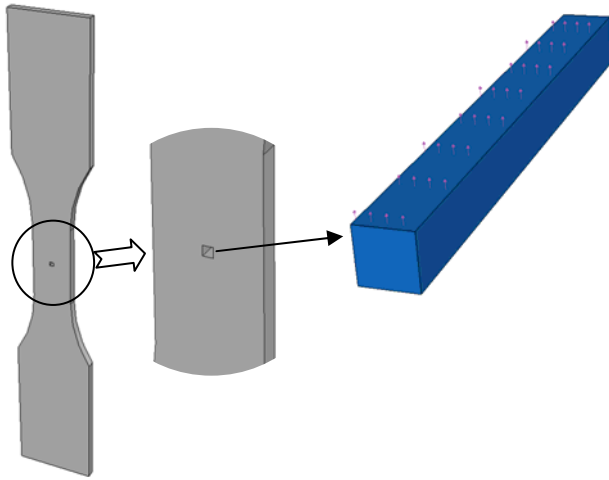
Figure 8. Schematic of dogbone specimen, uniform gage section and finite element geometry.

Prediction for retained residual stresses for a single mechanical loading cycle are shown in Figure 9. The maximum applied stress of 900 MPa results in yielding during loading. Three specimens, tested at these conditions, are averaged and shown as a solid line representing the mean response with error bars displaying the range of the XRD measurements for both the axial and transverse residual stress profiles. The range in the XRD measurements is greatest in the region where the residual stress profile has the largest value of compressive residual stress. This is expected since the errors in depth measurement, and stress correction for material removal, are greatest in the shallow depth region.
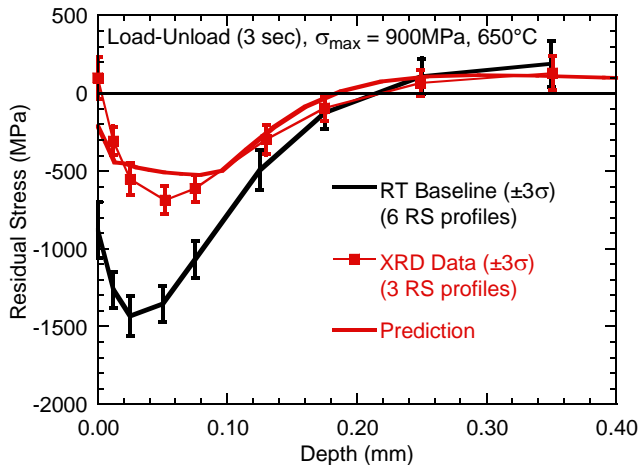

Figure 9. Prediction of retained residual stresses in shot-peened dogbone specimen from single load-unload cycle at 900 MPa and 650°C in IN100.

The prediction for the residual stress profiles, shown as the thick lines without symbols, capture the residual stress relaxation trend. Surprisingly, the data displays a small tensile surface residual stress. It has been demonstrated in the literature [37] that gross plastic straining of the entire cross section can reverse the residual stress profile, such that tensile residual stresses occur on the surface with compression in the center.

Prediction for retained residual stresses under sustained load (creep) loading, for 30 minutes, is shown in Figure 10. The maximum applied stress of 900 MPa results in yielding during loading. The prediction captures the surface residual stress and peak compressive stress. The measured profile displays a sharp point for the peak compressive residual stress, which is possibly an artifact of the XRD data reduction, and hence is not captured in the prediction.

For sustained loading of 10 hours, at the same applied maximum stress of 900 MPa, the retained residual stresses are less than that of the 30 minute profile as shown in Figure 11. Again, the experimental data exhibits a sharp peak in the compressive residual profile.
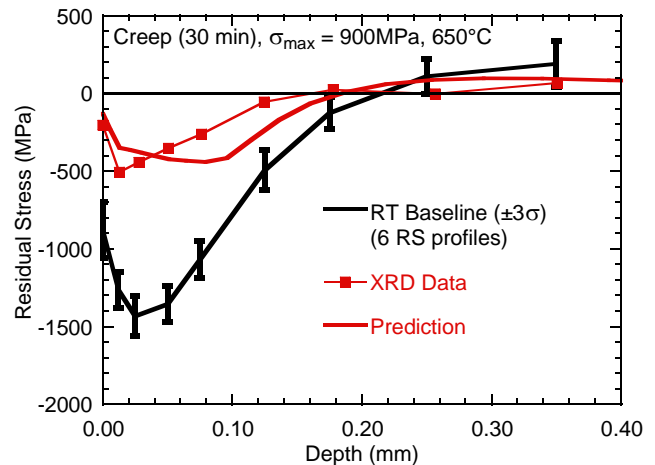

Figure 10. Prediction of retained residual stresses in shot-peened dogbone specimen from a 30 minute sustained load at 900 MPa and 650°C in IN100.
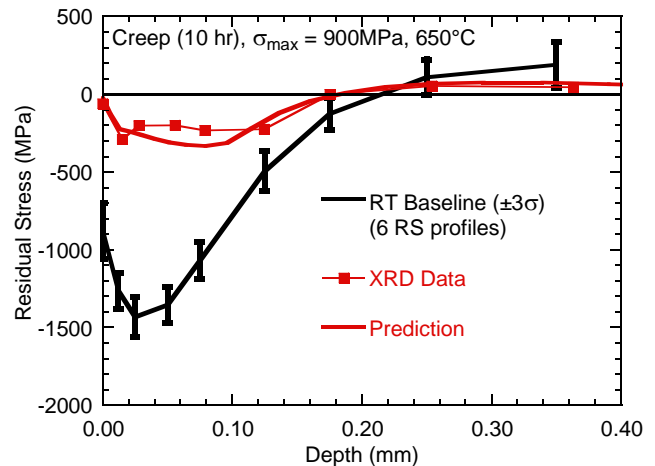

Figure 11. Prediction of retained residual stresses in shot-peened dogbone specimen from a 10 hour sustained load at 900 MPa and 650°C in IN100.

Clearly sustained loading is more detrimental than the load-unloading cycle to retained compressive residual stresses for applied stresses that develop plastic strain during loading. Furthermore, sustained loading continues to relax residual stresses with increasing creep time. Although significant relaxation of

compressive residual stresses occurs during creep relative to that of the load-unload cycle, the surface residual stress remains compressive. This is relatively surprising since analysis of the creep strain data for the 10 hour creep test revealed that the specimen was in tertiary creep and close to failure when the test was stopped.

Conclusions

A new coupled creep-plasticity model that incorporates plastic strain and yield surface state variables has been developed, and used successfully for predicting residual stress relaxation in shot-peened IN100. This model reflects the correct dominant deformation mechanism identified for relaxation of shot-peened residual stresses in this alloy and therefore provides the capability to model relaxation of other surface treatment processes such as LSP and LPB. Creep and plasticity are identified and modeled as different deformation mechanisms, coupled through state variables representing the evolution of the microstructure during deformation. This treatment is contrary to unified models that treat plasticity and creep as the same deformation mechanism grouped into a single rate equation. The coupled creep-plasticity approach facilitates incorporation of other creep deformation mechanisms into the model without additional extensive experimental testing and calibration.

Tensile and creep tests have been completed to characterize the baseline IN100 material at room and elevated temperature. Creep tests with prior room temperature prestrain demonstrate the effect plastic strain has on primary and secondary creep rate behavior. The proposed model has been demonstrated to give accurate predictions for stress relaxation under complex loading histories.

Acknowledgements

References

1. Happ, M. B., "Shot Peening Bolt Holes in Aircraft Engine Hardware," Proceedings Second International Conference on Shot Peening, 1984, pp. 43.
2. Vukelich, S., Berkley, S., Russ, S., and Bradley, E. F., "Residual stress measurement and its application to achieve predicted full life potential of low cycle fatigue (LCF) engine disks," The 9th International Symposium on Transport Phenomena and Dynamics of Rotating Machinery, Honolulu, Hawaii, February 2002.
3. Prevéy, P., Hornbach, D., and Mason, P., "Thermal residual stress relaxation and distortion in surface enhanced gas turbine engine components," Proceedings of the 17th Heat Treating Society Conference and Exposition and the 1st International Induction Heat Treating Symposium, Eds. D.L. Milam et.al., ASM Materials Park, OH, 1998, pp. 3-12.
4. Gabb, T. P., Telesman, J., Kantos, P. T., Bonacuse, P. J., Barrie, R. L., and Hornbach, D. J., "Stress Relaxation in Powder Metallurgy Superalloy Disks," TMS Letters, The Minerals, Metals & Materials Society, 2004.
5. Ahmad, J., Chandu, S., Kroupa, J., and Prevéy, P., "An assessment of residual stresses induced by surface treatments," Proceedings of the 6th National Turbine Engine High Cycle Fatigue Conference, HCF 2001, Jacksonville, FL., March 2001.
6. Cao, W., Khadhraoui, M., Brenier, B., Guédou, J. Y., and Castex, L., "Thermomechanical relaxation of residual stress in shot peened nickel base superalloy," Material Science and Technology, Vol. 10, November 1994, pp. 947-954.
7. Holzapfel, H., Schulze, V., Vöhringer, O., and Macherauch, E. "Residual stress relaxation in an AISI 4140 steel due to quasistatic and cyclic loading at higher temperatures," Material Science and Engineering A248, 1998, pp. 9-18.
8. Prevéy, P., "The Effect of Cold Work on the Thermal Stability of Residual Compression in Surface Enhanced 718," Proceedings of the 20th ASM Materials Solution Conference & Exposition, St. Louis, Missouri, 2000.
9. Buchanan, D. J., John, R., and Ashbaugh, N. E., "Thermal Residual Stress Relaxation in Powder Metal IN100 Superalloy," Journal of ASTM International, Vol. 3, No. 5, March 2006.
10. Chaboche, J. L., and Jung, O., "Application of a Kinematic Hardening Viscoplasticity Model with Thresholds to the Residual Stress Relaxation," International Journal of Plasticity, Vol. 13, No. 10, 1998, pp. 785-807.
11. Evans, R. W., and Wilshire, B., Creep of Metals and Alloys, The Institute of Metals, London, 1985.
12. Schoeck, G., "Theories of Creep," in Mechanical Behavior of Materials at Elevated Temperatures, Ed. J. E. Dorn, McGraw-Hill Book Company, Inc., New York, 1961, pp. 79-107.
13. Ashby, M. F., "A First Report on Deformation-Mechanism Maps," Acta Metallurgica, Vol. 20, July 1972, pp. 887-897.
14. Nowick, A. S., and Machlin, E. S., "Quantitative Treatment of the Creep of Metals by Dislocation and Rate Process Theories," National Advisory Committee for Aeronautics (NACA), Technical Note No. 1039, April 1946.
15. Weertman, J., "Theory of Steady-State Creep Based on Dislocation Climb," Journal of Applied Physics, Vol. 26, No. 10, October 1955, pp. 1213-1217.
16. Kachanov, L. M., "Time of the Rupture Process Under Creep Conditions," Izv. Akad. Nauk. SSR, Otd Tekh., Nauk No. 8, 1958, pp. 26-31.
17. Rabotnov, Y. N., Creep Problems in Structural Members, North Holland, Amsterdam, 1969.
18. Chaboche, J. L., "Continuum Damage Mechanics: Part I – General Concepts," Journal of Applied Mechanics, Vol. 55, March 1988, pp. 59-64.
19. Chaboche, J. L., "Continuum Damage Mechanics: Part II – Damage Growth, Crack Initiation, and Crack Growth," Journal of Applied Mechanics, Vol. 55, March 1988, pp. 65-72.
20. Sanders, D. R., "A Comparison of Several Creep Constitutive Theories for the Prediction of Elastic-Plastic-Creep Response and Their Application to Finite Element Analysis," Ph.D. Thesis, Texas A&M University, 1986.
21. McLean, M. and Dyson, B. F., "Modeling the Effects of Damage and Microstructural Evolution on the Creep

Behavior of Engineering Alloys," Journal of Engineering Materials and Technology, Vol. 122, July 2000, pp. 273-278.

22. Dyson, B. F., "Use of CDM in Materials Modeling and Component Creep Life Prediction," Journal of Pressure Vessel Technology, Vol. 122, August 2000, pp. 281-296.

23. Sondhi, S. K., Dyson, B. F., and McLean, M. "Tension-Compression creep asymmetry in a turbine disc superalloy: roles of internal stress and thermal ageing," Acta Materialia, 52, 2004, pp. 1761-1772.

24. Basoalto, H., Sondhi, S. K., Dyson, B. F., and McLean, M. "A Generic Microstructure-Explicit Model of Creep in Nickel-Base Superalloys," Superalloys 2004, Eds. K. A. Green, T. M. Pollock, H. Harada, T. E. Howson, R. C. Reed, J. J. Schirra and S. Walston, The Minerals, Metals, & Materials Society, 2004, pp. 897-906.

25. Bodner, S. R., "Constitutive Equations for Elastic-Visocplastic Strain-Hardening Materials," Journal of Applied Mechanics, Transactions of the ASME, June 1975, pp. 385-389.

26. Walker, K., "Research and Development Program for Nonlinear Structural Modeling with Advanced Time-Temperature Dependent Constitutive Relationships," NASA Contractor Report, NASA-CR-165533, 1981.

27. Ramaswamy, V. G., "A Constitutive Model for the Inelastic Multiaxial Cyclic Response of a Nickel Base Superalloy René 80," NASA Contractor Report 3998, 1986.

28. Robinson, D. N., "A Unified Creep-Plasticity Model for Structural Metals at High Temperature," ORNL TM-5969, October, 1978.

29. Miller, A. K., "An Inelastic Constitutive Model for Monotonic, Cyclic, Creep Deformation: Part I – Equations Development and Analytical Procedures; Part II – Applications to Type 304 Stainless Steel," Trans. ASME Journal of Engineering Materials and Technology, Vol. 96, 1976, pp. 97.

30. Dodds, R. H., "Numerical Techniques for Plasticity Computations in Finite Element Analysis," Computers & Structures, Vol. 26, No. 5, 1987, pp. 767-779.

31. Li, K., Ashbaugh, N. E., and Rosenberger, A. H., "Crystallographic Initiation of Nickel-Base Superalloy IN100 at RT and 538°C Under Low Cycle Fatigue Conditions," Superalloys 2004, Eds. K. A. Green, T. M. Pollock, H. Harada, T. E. Howson, R. C. Reed, J. J. Schirra, and S. Walston, TMS, 2004, pp. 251-258.

32. Davies, P. W., Finniear, T. C., and Wilshire, B., "The Effect of Compressive Prestrain on the Creep and Fracture Properties of Pure Nickel at 500°C," Journal of the Institute of Metals, Vol. 91, 1963, pp. 289-292.

33. Parker, J. D., and Wilshire, B., "The Effects of Prestrain on the Creep and Fracture Behavior of Polycrystalline Copper," Material Science and Engineering, Vol. 43, 1980, pp. 271-280.

34. Burt, H., Elliott, I. C., and Wilshire, B., "Effects of room-temperature prestrain on creep-fracture behavior of Nimonic 105," Metal Science, Vol. 15, September 1981, pp. 421-424.

35. Armstrong, P. J., and Frederick C. O., "A Mathematical Representation of the Multiaxial Baushhinger Effect," CEGB Report RD/B/N731, Berkeley Nuclear Laboratories, Berkeley, UK, 1966.

36. Braisted, W. R., and Brockman, R. A., Laser Shock Peening Analytical Development, UDRI-TR-1999-47, August 1999.

37. Kirk, D., "Effects of Plastic Straining on Residual Stresses Induced by Shot-Peening," Proceedings of the Third International Conference on Shot Peening, Eds. H. Wohlfahrt, R. Kopp and O. Vöhringer, Garmisch-Partenkirchen (FRG), 1987, pp. 213-220.

38. Buchanan, D. J., Ph.D. thesis, University of Dayton, 2007.